ICARUS **120,** 1–19 (1996)
ARTICLE NO. 0032

Galileo's Encounter with 243 Ida: An Overview of the Imaging Experiment

MICHAEL J. S. BELTON

National Optical Astronomy Observatories, Tucson, Arizona 85719
E-mail: belton@noao.edu

CLARK R. CHAPMAN

Planetary Science Institute, Tucson, Arizona 85705

KENNETH P. KLAASEN

Jet Propulsion Laboratory, California Institute of Technology, Pasadena, California 91109

ANN P. HARCH, PETER C. THOMAS, AND JOSEPH VEVERKA

Center for Radiophysics and Space Research, Cornell University, Ithaca, New York 14853

ALFRED S. MCEWEN

United States Geological Survey, Flagstaff, Arizona 86001

AND

ROBERT T. PAPPALARDO

Department of Geology, Arizona State University, Tempe, Arizona 85287

Received May 15, 1995; revised July 31, 1995

We provide an overview of the execution, data, and results of the solid state imaging (SSI) experiment at the encounter of the Galileo spacecraft with the asteroid 243 Ida. Ninety-six images of the asteroid, representing 18 time samples during a rotation period (4.633 h), were transmitted to Earth as a result of the UT 1993 August 28.70284 encounter. This provided coverage of ~95% of the surface and achieved ground resolutions as high as 25 m/pixel. Coverage of most of Ida's surface is available in four colors, with limited regions in five colors, at resolutions up to 105 m/pixel. A natural satellite of Ida, called Dactyl, was discovered in a prograde (with respect to Ida's spin), near-equatorial, orbit moving slowly (~ 6 m/sec) with a separation of 85 km from Ida.

Ida's shape is highly irregular; by comparison, Dactyl's global topography is quite smooth. The best fit ellipsoid to Ida's shape has principal dimensions 59.8 × 25.4 × 18.6 km, mean radius 15.7 km, and volume 16,100 ± 1900 km^3. Dactyl's mean radius is only 0.7 km. Ida's spin axis (right ascension: 348.76° ± 7.5°; declination: 87.10° ± 0.4°; J2000) was found to align with the principal axis of inertia to within the error of measurement. This is consistent with a homogeneous density distribution. Dactyl's rotation rate is unknown, but its long axis was pointed in the direction of Ida at the time of observation, suggesting synchronism of its orbital motion and spin. Constraints on Dactyl's orbit yield 4.2 ± 0.6 × 10^{19} g for Ida's mass and 2.6 ± 0.5 g/cm^3 for its bulk density. Unless Ida's bulk porosity is exceptionally high, Ida has moderate to low NiFe content.

Subtle color variations across the surface of Ida are associated with fresh craters, but, unlike the case for Asteroid 951 Gaspra, are not correlated with topographic features such as ridges. This difference may be a reflection of a deeper and/or more mobile regolith on Ida. Dactyl's spectral reflectance is similar to, but quantitatively distinct from the surface of Ida itself. This difference may reflect compositional differences between Dactyl and Ida, which in turn may have originated in an only partially differentiated Koronis parent body.

Results on the origin, collisional history, and geology of Ida and Dactyl are the subject of many of the papers in this special issue. There is general agreement that these asteroids originated in the catastrophic breakup of the Koronis parent body and that the formation of asteroid–satellite systems may be relatively common in such events. The age and collisional history of the pair present a dilemma: using standard interpretations of the cratering record on Ida's surface, an age > 1 byr. is indicated. However, the lifetime of Dactyl against collisional disruption

0019-1035/96 $18.00

is many times less than this. Novel ideas are presented concerning the collisional history of these two small objects that may resolve this dilemma. These ideas result from analysis of the geological record on the surface of Ida, Dactyl, and, by comparison, Gaspra—all of which are examined in this special issue.

The execution of the Galileo flybys of Gaspra, Ida, and Dactyl provide important lessons for future flybys of small bodies. We present our views on the limitations faced by the Galileo imaging experimenters and indicate how future missions can be made more quantitative and productive through the application of innovative electronic control systems and detector technology.

INTRODUCTION

Galileo's encounter with the asteroid 243 Ida occurred on August 28, 1993, at 16:52:04.7 UTC, on the final leg of the VEEGA trajectory to Jupiter (D'Amario *et al.* 1989). Ida, the second asteroid to be visited by the Galileo spacecraft, is a member of the Koronis family situated in the outer part of the belt (Table I). Groundbased observations (Binzel *et al.* 1993a) showed that it is highly elongated, but its shape and spin axis were not unambiguously determined. The spin period (4.633632 ± 0.000007 hr), retrograde sense of rotation, and globally integrated photometric properties are accurately known. Unlike 951 Gaspra, the first asteroid to be encountered by Galileo (cf. Veverka *et al.* 1994, and other papers in a special issue of *Icarus*, Vol. **107**, 1994), which is an olivine rich S-type asteroid, the near-infrared spectrum of Ida is more typical of S-types that have stronger indications of pyroxene in its spectrum (Binzel *et al.* 1993).

The scientific objectives of the SSI (solid state imaging) experiment at Ida were: (1) to fully characterize the shape and rotation state, (2) to obtain images with the highest possible spatial resolution at high solar incidence angle for the investigation of geologic and evolutionary processes, and (3) to obtain color and photometrically calibrated images for the investigation of microphysical and compositional properties of surface materials. The SSI Camera and its performance characteristics and filters are described in Belton *et al.* (1992). These scientific objectives were similar to those in an earlier Galileo encounter with Gaspra. However, the successful experience at Gaspra led to a goal of increased performance. Thus, the sequence at Ida included a high-risk pointing and mosaicking strategy to obtain images with spatial resolution approaching 25 m/pixel at the time of closest approach. This attempt to obtain images with more than twice the spatial resolution than was achieved at Gaspra was partially successful.

Certain intrinsic properties of Ida promised, and have yielded, a significantly increased science return in terms of a comparison with Gaspra: (1) since Ida is twice as large as Gaspra and spins twice as rapidly, the range of geologic processes on the surface was expected to be intrinsically greater and full rotational coverage of the surface could be obtained at higher spatial resolution; (2) since Ida is a member of the dynamically compact Koronis family, orbiting the Sun toward the outer edge of the belt, and Gaspra is near the inner edge, in the diffuse Flora family, their surfaces might be expected to show contrasting collisional histories; and (3) although both asteroids are in the same broad S taxonomic class, Ida is spectrally distinct from Gaspra, which is olivine-rich. Thus, new insights into the origin of taxonomic differences were expected from a comparative study.

Initial results on shape and surface geology, based on the first five high- resolution frames returned in 1993 have been published by Belton *et al.* (1994). Initial results concerning Ida's satellite, Dactyl, were published by Belton *et al.* (1995) and Chapman *et al.* (1995a). The 16 papers in this special issue contain detailed analyses of the entire data set. This contribution presents an overview of some of the major issues and results expressed in these papers and provides a detailed description of essential aspects of the encounter and data set that are common to each.

THE ENCOUNTER AND DATA ACQUISITION STRATEGY

The geometry of the encounter is shown in Fig. 1 and the parameters defining the flyby are collected in Table I. The spacecraft passed almost directly over the south pole of the asteroid crossing over the morning terminator. at high southern latitudes. For the highest resolution sequences over the terminator, the phase angle varied from 20.4° to 112.2° (Table IIA). Ground resolutions up to 25 m/pixel were achieved for geologic studies; up to 105 m/pixel was achieved for color studies of the surface.

The data acquisition sequence at Ida lasted slightly longer than one Ida rotation period (Table I). A total of 150 images was recorded representing 21 time samples of the rotation. Approximately 95% of the surface of Ida was covered and the imaging sequence was fully integrated with that of the near–infrared mapping spectrometer (NIMS) instrument which obtained complementary near-IR spectral data. Table IIB (together with IIA) shows how the shape and color coverage (Fig. 2a) was built-up on approach and how the sequence abruptly changed to high-resolution imaging at about −10 minutes (∼8000 km range).

Several high-resolution mosaics were acquired; the large number of frames devoted to these were needed to cover the ephemeris uncertainties of Ida relative to the spacecraft. The most important of these was the HIRES mosaic that was designed with a 95% probability of capture of the entire illuminated face of Ida, without gores, at a spatial resolution of ∼35 m/pixel (Fig. 2b). This is a considerably

TABLE I
Parameters for 243 Ida, Dactyl, and the Galileo Encounter

Name	Parameter	Value	Reference*
Galileo encounter			
	Encounter date	UTC 1993 Aug 28 16:52:04.7	1
	Closest approach distance	2391.2 km	1
	Flyby speed	12.38 $\mathrm{km.sec^{-1}}$	1
	Approach phase angle	19.17 deg (at E-1 day) (varies during encounter)	1
	# of images obtained/returned	150/96	1
	Best resolution	25 m.pixel-1	
243 Ida orbital properties			
	Semi-major axis	2.864 AU	1
	Eccentricity	0.04311	1
	Inclination	1.371 (with respect to ecliptic)	1
	Orbital period	1770.1 d	1
243 Ida physical properties			
	Period and sense of spin	4.633632 +/- 0.000007 hr; retrograde	2,3
	Right Ascension and Declination of spin pole (J2000)	RA=348°.76 +/- 7°.5 Dec=87°.10 +/- 0°.4	3
	Mean radius	15.7 km	4
	Volume	16,100 +/- 1900 $\mathrm{km^3}$	4
	Mass	4.2 x 10^{19}g	5
	Ratio of maximum-to-minimum Moments of inertia	3.7	4 (assumes homogeneity)
	Range of surface gravity	0.31 - 1.1 $\mathrm{cm.s^{-2}}$	4
	Bulk density	2.6 +/- 0.5 $\mathrm{g.cm^{-3}}$	5
	Maximum & Minimum Dimensions	55.8, 14.8 km	4
	Axial diameters (best fit ellipsoid)	59.8 x 25.4 x 18.6 km	4
	Visual geometric albedo	0.21 +0.03/-0.01	6
	Taxonomic group	S	2
1993 (243) 1 Dactyl Physical and Orbital Properties			
	Mean radius	0.7 km	7
	Axial diameters	1.6 x 1.4 x 1.2 km	7
	Volume	~1.4 $\mathrm{km^3}$	7
	Approximate mass (same bulk density as Ida)	~3.7 x 10^{15} g	7,5
	Spin period	> 8 h (possibly synchronous with orbital period ?)	7
	Approximate surface gravity	~0.05 $\mathrm{cm.s^{-2}}$	7,5
	Visual geometric albedo	0.20	8
	Taxonomic group	S	8
	Distance from Ida at encounter	85 km	5
	Orbital Period at Galileo encounter epoch	~37 h (?) (> 24.7 h)	5
	Orbital speed at encounter	6 m/sec	5
	Orbital inclination	172°	5
	Sense of orbital motion	Retrograde (with respect to orbital motion)	5

* References:

1. Antreasian, P.G., F.T. Nicholson, P.H. Kallemeyn, S. Bhaskaran, R.J. Haw, and P. Halamek 1994. JPL IOM GLL.NAV-94-65, 7 July.
2. Binzel *et al.*, 1993. *Icarus*, 105, 310-325.
3. Davies *et al.*, 1995. *Icarus*, this issue.
4. Thomas *et al.*, 1995. *Icarus*, this issue.
5. Belton *et al.*, 1995. *Icarus*, this issue.
6. Helfenstein *et al.*, 1995. *Icarus*, this issue.
7. Veverka *et al.*, 1995*a*. *Icarus*, this issue.
8. Veverka *et al., 1995b*. *Icarus*, this issue.

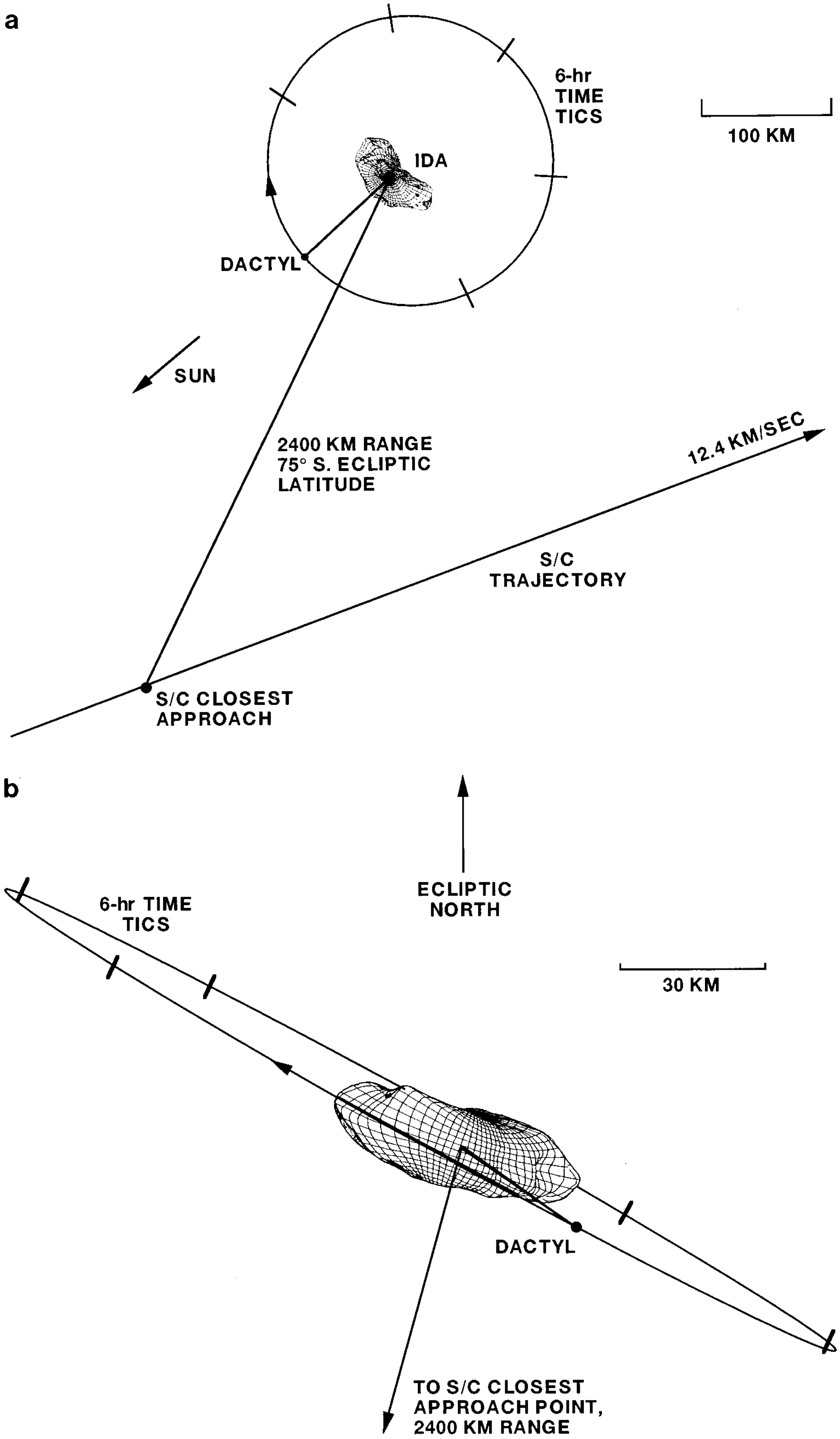

FIG. 1. The Galileo flyby trajectory at Ida showing the shape and orientation of Ida and the position of Dactyl at the time of encounter. The orbit of Dactyl assumes that the GM of Ida is 0.0028 $\mathrm{km}^3\,\mathrm{sec}^{-2}$ which corresponds to the mid range of the possible values (Belton *et al.* 1995). (a) Viewed from the direction of Ida's north pole. The spacecraft trajectory and closest approach point are far below, ~2000 km, below the plane of the figure over about 80°S latitude on Ida. Ida and Dactyl both rotate clockwise in this view. (b) Viewed from the direction of the approach asymptote.

TABLE IIA
Geometry of Galileo Images of 243 Ida and 1993 (243)1 Dactyl

Image #	Phase (deg.)	Range (km)	Resolution (m.pixel^{-1})	Latitude (deg.)	Longitude (deg.)
202530700	19.5	240,429	2,443	6.76	5.87
202533000	19.5	223,151	2,267	6.71	35.99
202533045	19.5	222,775	2,263	6.71	36.64
202533100	19.5	222,399	2,260	6.71	37.30
202533145	19.5	222,024	2,256	6.71	37.95
202533200	19.5	221,648	2,252	6.71	38.61
202533245	19.5	221,272	2,248	6.71	39.26
202535300	19.5	205,874	2,092	6.66	66.11
202537600	19.5	188,597	1,916	6.60	96.23
202539900	19.6	171,319	1,741	6.53	126.35
202539945	19.6	170,944	1,737	6.53	127.00
202540000	19.6	170,567	1,733	6.52	127.66
202540045	19.6	170,192	1,729	6.52	128.32
202540100	19.6	169,816	1,725	6.52	128.97
202540145	19.6	169,441	1,722	6.52	129.63
202542200	19.6	154,043	1,565	6.44	156.47
202544500	19.7	136,767	1,390	6.33	186.60
202546800	19.7	119,491	1,214	6.18	216.73
202546845	19.7	119,116	1,210	6.18	217.39
202546900	19.7	118,739	1,206	6.18	218.04
202546945	19.7	118,364	1,203	6.17	218.70
202547000	19.7	117,988	1,199	6.17	219.35
202547045	19.7	117,613	1,195	6.16	220.01
202549100	19.8	102,217	1,039	5.99	246.87
202549145	19.8	101,841	1,035	5.99	247.52
202549200	19.8	101,465	1,031	5.98	248.18
202549245	19.8	101,089	1,027	5.98	248.83
202549300	19.8	100,714	1,023	5.97	249.49
202551400	19.9	84,944	863	5.72	277.01
202551445	19.9	84,568	859	5.71	277.67
202551500	19.9	84,193	855	5.71	278.32
202551545	19.9	83,817	852	5.70	278.98
202551600	19.9	83,442	848	5.69	279.64
202553700	20.1	67,674	688	5.31	307.18
202553745	20.1	67,299	684	5.30	307.83
202553800	20.1	66,923	680	5.29	308.49
202553845	20.1	66,548	676	5.28	309.14
202553900	20.1	66,172	672	5.26	309.80
202553945	20.1	65,797	668	5.25	310.46
202554800	20.2	59,417	604	5.03	321.61
202554845	20.2	59,041	600	5.02	322.27
202554900	20.2	58,665	596	5.00	322.92
202554945	20.2	58,290	592	4.99	323.58
202555000	20.2	57,914	588	4.97	324.24
202555045	20.2	57,540	585	4.96	324.89
202556000	20.4	50,410	512	4.62	337.37
202556045	20.4	50,035	508	4.60	338.03
202556100	20.4	49,659	505	4.58	338.69
202556145	20.4	49,284	501	4.56	339.34
202556200	20.4	48,909	497	4.54	340.00
202556245	20.4	48,534	493	4.52	340.66
202557100	20.6	42,158	428	4.09	351.84
202557145	20.7	41,783	425	4.06	352.49
202557200	20.7	41,407	421	4.03	353.15
202557245	20.7	41,032	417	4.00	353.81
202557300	20.7	40,657	413	3.97	354.47
202557345	20.7	40,282	409	3.94	355.13
202558300	21.1	33,161	337	3.22	7.65
202558345	21.1	32,787	333	3.17	8.31
202558400	21.1	32,411	329	3.12	8.97
202558445	21.2	32,037	325	3.07	9.63
202558500	21.2	31,662	322	3.02	10.29

TABLE IIA—*Continued*

Image #	Phase (deg.)	Range (km)	Resolution (m.pixel^{-1})	Latitude (deg.)	Longitude (deg.)
202558545	21.2	31,288	318	2.97	10.95
202559400	21.8	24,926	253	1.85	22.22
202559445	21.8	24,553	249	1.77	22.88
202559500	21.9	24,178	246	1.69	23.55
202559545	21.9	23,804	242	1.60	24.21
202559600	22.0	23,431	238	1.50	24.88
202559645	22.1	23,057	234	1.41	25.54
202560500	23.4	16,720	170	-0.84	36.94
202560545	23.5	16,348	166	-1.03	37.61
202560600	23.6	15,976	162	-1.23	38.29
202560645	23.8	15,604	159	-1.43	38.97
202560700	23.9	15,233	155	-1.65	39.65
202560745	24.1	14,863	151	-1.87	40.33
202561278	26.4	10,931	111	-5.23	47.71
202561300	26.5	10,826	110	-5.35	47.91
202561313	26.5	10,721	109	-5.48	48.12
202561326	26.6	10,616	108	-5.61	48.32
202561339	26.7	10,511	107	-5.74	48.52
202561352	26.8	10,407	106	-5.87	48.73
202561365	26.9	10,303	105	-6.00	48.93
202561378	27.0	10,198	104	-6.14	49.13
202561400	27.1	10,094	103	-6.29	49.34
202561413	27.2	9,990	101	-6.43	49.54
202561426	27.4	9,886	100	-6.58	49.74
202561439	27.5	9,781	99	-6.73	49.95
202561452	27.6	9,677	98	-6.88	50.16
202561465	27.7	9,573	97	-7.04	50.36
202561478	27.8	9,470	96	-7.20	50.57
202561500	27.9	9,366	95	-7.37	50.78
202561513	28.1	9,262	94	-7.54	50.98
202561526	28.2	9,158	93	-7.71	51.19
202561539	28.3	9,055	92	-7.88	51.40
202561552	28.5	8,951	91	-8.06	51.61
202561565	28.6	8,848	90	-8.25	51.82
202561578	28.8	8,745	89	-8.44	52.03
202561700	30.1	7,904	80	-10.17	53.77
202561745	30.8	7,547	77	-11.02	54.53
202561800	31.5	7,191	73	-11.96	55.30
202561845	32.4	6,838	69	-13.00	56.08
202561900	33.3	6,488	66	-14.15	56.88
202561945	34.4	6,140	62	-15.44	57.70
202562000	35.6	5,796	59	-16.87	58.54
202562045	37.0	5,456	55	-18.49	59.41
202562152	40.6	4,764	48	-22.59	61.33
202562165	41.2	4,671	47	-23.25	61.61
202562178	41.8	4,579	47	-23.93	61.89
202562200	42.4	4,488	46	-24.64	62.18
202562213	43.1	4,398	45	-25.38	62.48
202562226	43.8	4,308	44	-26.15	62.78
202562239	44.5	4,219	43	-26.95	63.08
202562252	45.3	4,131	42	-27.78	63.40
202562265	46.1	4,044	41	-28.66	63.72
202562278	46.9	3,958	40	-29.57	64.05
202562300	47.8	3,873	39	-30.52	64.38
202562313	48.7	3,789	38	-31.51	64.73
202562326	49.6	3,707	38	-32.55	65.09
202562339	50.6	3,625	37	-33.63	65.46
202562352	51.7	3,545	36	-34.76	65.85
202562365	52.8	3,467	35	-35.95	66.25
202562378	53.9	3,390	34	-37.18	66.66
202562400	55.1	3,315	34	-38.48	67.10
202562413	56.4	3,241	33	-39.83	67.55
202562426	57.7	3,170	32	-41.24	68.03
202562439	59.1	3,100	31	-42.72	68.54
202562452	60.6	3,033	31	-44.27	69.08

TABLE IIA—*Continued*

Image #	Phase (deg.)	Range (km)	Resolution (m.pixel^{-1})	Latitude (deg.)	Longitude (deg.)
202562465	62.1	2,968	30	-45.88	69.65
202562478	63.7	2,906	30	-47.55	70.26
202562500	65.4	2,846	29	-49.30	70.93
202562513	67.1	2,790	28	-51.12	71.65
202562526	68.9	2,736	28	-53.02	72.44
202562539	70.8	2,685	27	-54.98	73.31
202562552	72.8	2,638	27	-57.01	74.28
202562565	74.8	2,595	26	-59.10	75.37
202562578	76.9	2,555	26	-61.25	76.62
202562600	79.1	2,519	26	-63.46	78.06
202562613	81.3	2,488	25	-65.72	79.76
202562626	83.6	2,460	25	-68.01	81.79
202562639	85.9	2,437	25	-70.33	84.27
202562652	88.3	2,419	25	-72.64	87.39
202562665	90.7	2,405	24	-74.93	91.42
202562678	93.1	2,396	24	-77.16	96.84
202562700	95.6	2,392	24	-79.25	104.35
202562713	98.0	2,392	24	-81.09	115.06
202562726	100.5	2,397	24	-82.49	130.37
202562739	102.9	2,408	24	-83.19	150.38
202562752	105.3	2,422	25	-82.98	171.56
202562765	107.6	2,442	25	-81.97	189.15
202562778	109.9	2,466	25	-80.44	201.86
202562800	112.2	2,494	25	-78.62	210.70

better performance than what was achieved at Gaspra (54 m/pixel). The highest resolution ENCNTR mosaic was designed for a 50% probability of capture, the demands for onboard image storage being too large to accommodate higher probability. Only a small portion of Ida was actually imaged in the ENCNTR mosaic.

Shortly after the sequence began, the spacecraft experienced a control system anomaly that resulted in turning off the attitude control gyros and slewing the instrument scan platform to a safe position. Approximately 60° of asteroid rotation was lost due to mispointing of the scan platform prior to automatic recovery of the sequence.

DATA RETURN STRATEGY

The spacecraft's main communication antenna is improperly deployed. This resulted in the downlink (the data rate available to Earth) being restricted to only 40 bps (normal downlink rates would have been ~115 kbps). The large quantity of imaging data ($\sim 7 \times 10^8$ bits) that was acquired was therefore stored entirely on the spacecraft's tape recorder for later playback to Earth. The 40-bps data rate was available only for two periods (8/28/93–9/29/93 and 2/94–6/94). This factor, plus the need to minimize tape recorder usage prior to reaching the main mission objective of Jupiter and also to write SSI data from the comet Shoemaker–Levy 9 collision with Jupiter to the tape in July, 1994 (Chapman *et al.* 1995b, Neukum *et al.* 1995), resulted in only ~16% of the recorded SSI data (measured in bits written) being returned to Earth. Most of the unreturned data was background dark sky, although some color images of the Ida/Dactyl system were also sacrificed (cf. Table IIB).

The initial playback, immediately following encounter, was designed to locate the highest priority data and the high-resolution mosaics HIRES and ENCNTR, on the tape. A technique dubbed "jailbar search" was used in which only two or three image lines out of every 330 were extracted off the tape and returned to Earth from all 45 frames in these two mosaics. From these sparse image segments, together with the most probable Ida shape solutions determined from ground-based lightcurve data (cf. Thomas *et al.* 1996), it was possible to determine which images contained Ida and also make more accurate estimates of Ida's size, shape, and pole orientation. Using this information, the segments of frames (cf. Table IIB) containing Ida in these mosaics were selected for full playback.

Ida was slightly larger than expected and covered portions of five different frames of the HIRES mosaic (Fig. 2c). This single view of Ida required the entire Sept. 1993 playback period. Only a small segment of Ida's limb was found to be captured in the ENCNTR mosaic (Image 202562778) and return of these data was deferred to 1994.

The results of the initial playback and knowledge of the pointing anomaly fed into the planning for data return in 1994 and led to an unplanned, but fortunately implemented, adaptive strategy for the playback which would allow the early data to affect the content of later playback. The first data returned were jailbar searches of the color

TABLE IIB
Galileo Images of 243 Ida and 1993 (243)1 Dactyl

Observation Name	Image #	UTC Frame Start Time	Filter	Exposure (msec)	Gain State	Lines Returned
ROTATION1	202530700	93-240/11:28:27.000	CLEAR	8.33	2	136
	202533000	93-240/11:51:42.333	GREEN	66.67	2	0
	202533045	93-240/11:52:12.333	RED	50.00	2	0
	202533100	93-240/11:52:43.000	VIOLET	200.00	3	0
	202533145	93-240/11:53:13.000	7650	133.33	3	0
	202533200	93-240/11:53:43.666	9680	200.00	4	0
	202533245	93-240/11:54:13.666	8890	133.33	4	0
	202535300	93-240/12:14:57.666	CLEAR	8.33	2	0
	202537600	93-240/12:38:13.000	CLEAR	8.33	2	0
ROTATION2	202539900	93-240/13:01:28.333	GREEN	66.67	2	258
	202539945	93-240/13:01:58.333	RED	50.00	2	32
	202540000	93-240/13:02:29.000	VIOLET	200.00	3	134
	202540045	93-240/13:02:59.000	7650	133.33	3	30
	202540100	93-240/13:03:29.666	9680	200.00	4	268
	202540145	93-240/13:03:59.666	8890	133.33	4	134
	202542200	93-240/13:24:43.666	CLEAR	8.33	2	188
	202544500	93-240/13:47:58.933	CLEAR	8.33	2	124
ROTATION3	202546800	93-240/14:11:14.266	GREEN	66.67	2	138
	202546845	93-240/14:11:44.266	RED	50.00	2	24
	202546900	93-240/14:12:14.933	VIOLET	200.00	3	134
	202546945	93-240/14:12:44.933	7650	133.33	3	30
	202547000	93-240/14:13:15.599	9680	200.00	4	136
	202547045	93-240/14:13:45.599	8890	133.33	4	160
	202549100	93-240/14:34:29.499	GREEN	66.67	2	228
	202549145	93-240/14:34:59.599	VIOLET	200.00	3	37
	202549200	93-240/14:35:30.266	7650	133.33	3	0
	202549245	93-240/14:36:00.266	9680	200.00	4	0
	202549300	93-240/14:36:30.933	8890	133.33	4	0
	202551400	93-240/14:57:44.933	GREEN	66.67	2	134
	202551445	93-240/14:58:14.933	VIOLET	200.00	3	136
	202551500	93-240/14:58:45.599	7650	133.33	3	0
	202551545	93-240/14:59:15.599	9680	200.00	4	138
	202551600	93-240/14:59:46.266	8890	133.33	4	136
ROTATION4	202553700	93-240/15:21:00.266	GREEN	66.67	2	138
	202553745	93-240/15:21:30.266	RED	50.00	2	0
	202553800	93-240/15:22:00.933	VIOLET	200.00	3	134
	202553845	93-240/15:22:30.933	7650	133.33	3	0
	202553900	93-240/15:23:01.599	9680	200.00	4	132
	202553945	93-240/15:23:31.599	8890	133.33	4	134
	202554800	93-240/15:32:07.599	GREEN	66.67	2	136
	202554845	93-240/15:32:37.599	RED	50.00	2	0
	202554900	93-240/15:33:08.266	VIOLET	200.00	3	0
	202554945	93-240/15:33:38.266	7650	133.33	3	0
	202555000	93-240/15:34:08.933	9680	200.00	4	0
	202555045	93-240/15:34:38.933	8890	133.33	4	0
	202556000	93-240/15:44:15.599	GREEN	66.67	2	138
	202556045	93-240/15:44:45.599	RED	50.00	2	136
	202556100	93-240/15:45:16.266	VIOLET	200.00	3	136
	202556145	93-240/15:45:46.266	7650	133.33	3	0
	202556200	93-240/15:46:16.933	9680	200.00	4	136
	202556245	93-240/15:46:46.933	8890	133.33	4	136
	202557100	93-240/15:55:22.933	GREEN	66.67	2	136
	202557145	93-240/15:55:52.933	RED	50.00	2	0
	202557200	93-240/15:56:23.599	VIOLET	200.00	3	136
	202557245	93-240/15:56:53.599	7650	133.33	3	0
	202557300	93-240/15:57:24.266	9680	200.00	4	136
	202557345	93-240/15:57:54.266	8890	133.33	4	138
	202558300	93-240/16:07:30.933	GREEN	66.67	2	138
	202558345	93-240/16:08:00.933	RED	50.00	2	0
	202558400	93-240/16:08:31.599	VIOLET	200.00	3	136
	202558445	93-240/16:09:01.599	7650	133.33	3	0
	202558500	93-240/16:09:32.266	9680	200.00	4	138

TABLE IIB—*Continued*

Observation Name	Image #	UTC Frame Start Time	Filter	Exposure (msec)	Gain State	Lines Returned
ROTATION4 (continued)	202558545	93-240/16:10:02.266	8890	133.33	4	136
	202559400	93-240/16:18:38.266	GREEN	66.67	2	136
	202559445	93-240/16:19:08.266	RED	66.67	2	0
	202559500	93-240/16:19:38.933	VIOLET	200.00	3	0
	202559545	93-240/16:20:08.933	7650	200.00	3	0
	202559600	93-240/16:20:39.599	9680	200.00	4	0
	202559645	93-240/16:21:09.599	8890	133.33	4	0
FINROT	202560500	93-240/16:29:45.599	GREEN	66.67	2	268
	202560545	93-240/16:30:15.599	RED	66.67	2	0
	202560600	93-240/16:30:46.266	VIOLET	200.00	3	302
	202560645	93-240/16:31:16.266	7650	200.00	3	64
	202560700	93-240/16:31:46.933	9680	200.00	4	198
	202560745	93-240/16:32:16.933	8890	133.33	4	264
6COLOR(1X1)	202561278	93-240/16:37:42.266	GREEN	66.67	2	379
	202561300	93-240/16:37:50.933	RED	66.67	2	0
	202561313	93-240/16:37:59.599	VIOLET	200.00	3	424
	202561326	93-240/16:38:08.266	7650	200.00	3	379
	202561339	93-240/16:38:16.933	9680	200.00	4	375
	202561352	93-240/16:38:25.599	8890	200.00	4	372
6COLOR(2X2)	202561365	93-240/16:38:34.266	GREEN	66.67	2	0
	202561378	93-240/16:38:42.933	VIOLET	200.00	3	0
	202561400	93-240/16:38:51.599	9680	200.00	4	0
	202561413	93-240/16:39:00.266	8890	200.00	4	0
	202561426	93-240/16:39:08.933	GREEN	66.67	2	0
	202561439	93-240/16:39:17.599	VIOLET	200.00	3	0
	202561452	93-240/16:39:26.266	9680	200.00	4	0
	202561465	93-240/16:39:34.933	8890	200.00	4	0
	202561478	93-240/16:39:43.599	GREEN	66.67	2	0
	202561500	93-240/16:39:52.266	VIOLET	200.00	3	0
	202561513	93-240/16:40:00.933	9680	200.00	4	0
	202561526	93-240/16:40:09.599	8890	200.00	4	0
	202561539	93-240/16:40:18.266	GREEN	100.00	2	0
	202561552	93-240/16:40:26.933	VIOLET	200.00	3	0
	202561565	93-240/16:40:35.599	9680	200.00	4	0
	202561578	93-240/16:40:44.266	8890	200.00	4	380
IDACHEM	202561700	93-240/16:41:53.599	CLEAR	12.50	2	800
	202561745	93-240/16:42:23.599	CLEAR	12.50	2	800
	202561800	93-240/16:42:54.266	CLEAR	12.50	2	237
	202561845	93-240/16:43:24.266	CLEAR	12.50	2	138
	202561900	93-240/16:43:54.933	CLEAR	16.67	2	413
	202561945	93-240/16:44:24.933	CLEAR	16.67	2	800
	202562000	93-240/16:44:55.599	CLEAR	16.67	2	800
	202562045	93-240/16:45:25.599	CLEAR	16.67	2	25
HIRES	202562152	93-240/16:46:30.933	CLEAR	8.33	3	7
	202562165	93-240/16:46:39.599	CLEAR	8.33	3	10
	202562178	93-240/16:46:48.266	CLEAR	8.33	3	10
	202562200	93-240/16:46:56.933	CLEAR	8.33	3	10
	202562213	93-240/16:47:05.599	CLEAR	8.33	3	7
	202562226	93-240/16:47:14.266	CLEAR	8.33	3	10
	202562239	93-240/16:47:22.933	CLEAR	8.33	3	10
	202562252	93-240/16:47:31.599	CLEAR	8.33	3	5
	202562265	93-240/16:47:40.266	CLEAR	8.33	3	364
	202562278	93-240/16:47:48.933	CLEAR	8.33	3	238
	202562300	93-240/16:47:57.599	CLEAR	8.33	3	793
	202562313	93-240/16:48:06.266	CLEAR	8.33	3	744
	202562326	93-240/16:48:14.933	CLEAR	8.33	3	762
	202562339	93-240/16:48:23.599	CLEAR	12.50	3	797
	202562352	93-240/16:48:32.266	CLEAR	12.50	3	96
	202562365	93-240/16:48:40.933	CLEAR	12.50	3	88
	202562378	93-240/16:48:49.599	CLEAR	12.50	3	93
	202562400	93-240/16:48:58.266	CLEAR	12.50	3	6
	202562413	93-240/16:49:06.933	CLEAR	12.50	3	6

TABLE IIB—*Continued*

Observation Name	Image #	UTC Frame Start Time	Filter	Exposure (msec)	Gain State	Lines Returned
HIRES (continued)	202562426	93-240/16:49:15.599	CLEAR	12.50	3	798
	202562439	93-240/16:49:24.266	CLEAR	12.50	3	800
	202562452	93-240/16:49:32.933	CLEAR	12.50	3	6
	202562465	93-240/16:49:41.599	CLEAR	12.50	3	6
	202562478	93-240/16:49:50.266	CLEAR	12.50	3	6
	202562500	93-240/16:49:58.933	CLEAR	12.50	3	6
	202562513	93-240/16:50:07.599	CLEAR	12.50	3	6
	202562526	93-240/16:50:16.266	CLEAR	12.50	3	6
	202562539	93-240/16:50:24.933	CLEAR	12.50	3	6
	202562552	93-240/16:50:33.599	CLEAR	12.50	3	5
	202562565	93-240/16:50:42.266	CLEAR	12.50	3	4
ENCNTR	202562600	93-240/16:50:59.599	CLEAR	16.67	3	70
	202562613	93-240/16:51:08.266	CLEAR	25.00	3	9
	202562626	93-240/16:51:16.933	CLEAR	16.67	3	6
	202562639	93-240/16:51:25.599	CLEAR	25.00	3	50
	202562652	93-240/16:51:34.266	CLEAR	16.67	3	52
	202562665	93-240/16:51:42.933	CLEAR	16.67	3	6
	202562678	93-240/16:51:51.599	CLEAR	50.00	2	6
	202562700	93-240/16:52:00.266	CLEAR	50.00	2	195
	202562713	93-240/16:52:08.933	CLEAR	6.25	4	50
	202562726	93-240/16:52:17.599	CLEAR	8.33	4	5
	202562739	93-240/16:52:26.266	CLEAR	33.33	3	6
	202562752	93-240/16:52:34.933	CLEAR	33.33	3	6
	202562765	93-240/16:52:43.599	CLEAR	8.33	4	6
	202562778	93-240/16:52:52.266	CLEAR	8.33	4	799
	202562800	93-240/16:53:00.933	CLEAR	33.33	3	6

sequences acquired between −22 and −10 min. from encounter and of some of the early rotation data obtained on approach. It was during the examination of these data that, on Feb. 17, 1994, Dactyl, a natural satellite of Ida was discovered (Belton and Carlson 1994). This event led to full exercise of the adaptivity feature in the playback activities.

NOMENCLATURE

In Greek mythology, the infant Zeus was hidden in a cave on Mount Ida. Considering this, the IAU has designated that craters on Ida are to be named for caves and grottos of the world. Only one crater name, Afon, is currently approved by the IAU, and this crater serves as the origin of longitudes on Ida. All other names shown in Fig. 2c are only proposed, but have been consistently used in the papers included in this issue. Table III contains a list of such named craters and their locations.

Regions (*regii*) honor Johann Palisa, Ida's discoverer, and include names of the cities from which he observed. Ridges (*dorsa*) honor deceased Galileo team members and associates. The name of Ida's satellite, Dactyl, was proposed as a result of a Galileo project wide competition. The Dactyloi guarded the offspring of Zeus by Rhea and were wizards who came from Mount Ida in Crete. Dactyl's craters are named after individual Dactyls.

GLOBAL CHARACTERISTICS

Ida's highly irregular shape, spin, and global photometric and spectral properties were to some extent anticipated in the interpretation of ground-based telescopic data (cf. Binzel *et al.* 1993a). This work clearly showed the capabilities and the limitations of current techniques to invert, or confidently model, integrated lightcurves with only modest complexity and the observational degeneracy of the two possible spin states that arises for objects with low orbital inclination. The highly elongated (Table I), croissant-like shape detailed by Thomas *et al.* (1996) is the most irregularly shaped object yet imaged from a spacecraft. It is poorly fit by an ellipsoid, a shape often used in modeling small bodies. A waist-like structure divides Ida into two regions which show some differences in their cratering characteristics, but share many similarities. The correspondence of the observed spin axis to the minimum principle moment of inertia is evidence for approximate density homogeneity in the interior of the asteroid on the largest scales.

The orientation of the long axis of the asteroid in the HIRES mosaic immediately eliminated one of the two possible ground-based spin states. In Davies *et al.* (1996), the spin pole direction is precisely determined (Table 1) and a geodetic control net is established which is the basis of the latitude–longitude grid shown in Fig. 3. All of the papers in this issue refer to this system which is illustrated here for reference. We would have experienced difficulty in interpolating coordinate positions onto the surface without such a guide. The spin period determined by Binzel *et al.* (1993a) using ground-based techniques, was essential for establishing this system. In Simonelli *et al.* (1996), the shape, spin, and photometric properties of the surface (Helfenstein *et al.* 1996) are combined to recover the essence of the ground-based lightcurves.

Excellent imaging coverage of Dactyl was obtained primarily because of the satellite's fortuitous proximity to Ida, the near equatorial inclination of its orbit, and its low orbital speed. Veverka *et al.* (1996a,b) present the facts which have been gleaned from these images. Dactyl's smooth limb and modest ellipsoidal shape stand in stark comparison to Ida's angular appearance, which raises interesting questions regarding its origin or subsequent evolution in orbit (Chapman *et al.* 1995a, Geissler *et al.* 1996). Veverka *et al.* (1996a) also point out the fact that Phobos and Deimos are similarly smooth, a factor that should be considered in the interpretation of the origin of Dactyl's shape.

An important by-product of this, perhaps serendipitous, coverage of Dactyl was a useful constraint on the bulk density of Ida (Belton *et al.* 1996), thereby giving insight into its bulk porosity and composition (see below). The shape and stability of Dactyl's orbit is still far from understood and much remains that can be done, both observationally (with HST) and theoretically, to understand the enigmatic presence of this fascinating object.

COLLISIONAL HISTORY, CRATERS, AND GEOLOGY

Ida's initial formation as a separate body certainly resulted from breakup of the Koronis family parent body (Davis *et al.* 1996). A similar origin for Dactyl was proposed by Chapman *et al.* (1995a). Durda (1996) shows that formation of satellites and multiple contact structures is expected to occur commonly around the larger fragments of the parent asteroid in the aftermath of a catastrophic breakup.

Interpretation of Ida's bulk density of 2.6 ± 0.5 g cm^{-3} (Belton *et al.* 1995) and the large scale structural features that are seen on Ida (Thomas *et al.* 1996) depends significantly on the porosity and cohesive state of the interior of the asteroid. The upper and lower limits on the range of allowable bulk density are set by the necessity for Dactyl to have a long-lived orbit gravitationally bound to Ida (Belton *et al.* 1996) and uncertainties in the shape determination (Thomas *et al.* 1996). Is the interior completely "rubblized?" What is its *bulk* porosity? Is it a weakly cohesive collection of a few large fragments? Or is the interior largely a coherent splinter of rock? Asphaug *et al.* (1996) show, using hydrocode calculations, that currently recognized impact features would not be expected to have created heavy fracturing throughout the interior since intense fracturing occurs only to a depth approaching one crater diameter. However, in the region from the waist structure to Pola Regio (Fig. 2) where the largest craters are found, fracturing at depth could be extensive. In addition, Asphaug *et al.* point out that tensile shock waves generated during the formation of a possible large crater that remains as Vienna Regio and channeled through the body of the asteroid could further disrupt the interior beneath Pola Regio. A different view of the internal structure is offered by Davis *et al.* (1996) who argue on the basis of the observed shape of Ida that it could be a rubble pile.

Since Ida's formation, the evolution of its surface has been dominated by the effects of impacts (Asphaug *et al.* 1996, Chapman *et al.* 1996, Geissler *et al.* 1996, Sullivan *et al.* 1996). The large-scale shape of Ida has probably been modified by relatively large impact craters and spalls. A complete range of crater degradation states is present, from apparently pristine to barely recognizable. Diameter/depth ratios for fresh craters on Ida, as determined from photoclinometric profiles, are 6.5 : 1 (Sullivan *et al.* 1996), similar to previous results for Gaspra (Carr *et al.* 1994), but significantly greater (Sullivan *et al.* 1996) than the 5 : 1 ratios common on other rocky bodies. Sullivan *et al.* (1996) discuss the origin of these shallower pristine craters which could be due to either whole body "ringing" from energetic impacts that lead to a more complete collapse of the transient cavity or a more rapid deterioration of their rims (Carr *et al.* 1994), or the lesser effects of gravity on the strength and compaction of the surface layers on such small bodies.

There is considerable evidence for an impact-generated regolith on Ida. Ida's photometric properties are consistent with a particulate regolith and color variations are consistent with regolith maturity variations (Helfenstein *et al.* 1996). Mechanical and dynamical models indicate that most ejecta from craters larger than about 1 km diameter will reaccrete rather than being lost from the system (Asphaug *et al.* 1996, Geissler *et al.* 1996). Several morphologic features seen at high resolution are best explained as related to the regolith (Sullivan *et al.* 1996): (1) mass-wasting scars and albedo streaks oriented down local slopes, interpreted as due to mass wasting in the regolith; (2) the presence of isolated positive relief features, which are interpreted as ejecta blocks (the presumed largest components of a size distribution of finer particulates); and (3) grooves, interpreted as the surface expressions in the regolith of deep fractures.

PHOTOMETRY AND COLORS: COMPOSITION AND REGOLITH PROPERTIES

Helfenstein *et al.* (1996) find that there are two basic color units on Ida: Terrains A (typical of most of the surface

FIG. 2. (a) A color rendition of various views of Ida adjusted to the same scale to show the interplay of lighting, albedo, and color over the surface as the encounter progressed. The images are arranged from left to right in order of decreasing range and with the most distant at the top left and the closest at the bottom right. In the most distant images the south ecliptic pole is approximately oriented toward the top of the figure. As the encounter proceeds the view from the spacecraft dips to southern latitudes on the asteroid and the projected direction to the ecliptic south pole slowly rotates clockwise. These pictures, which also serve to illustrate the contorted shape of the asteroid, are built-up of triplets of images taken through the 1-μm (Red), GRN (Green), and VLT (Blue) filters (Belton *et al.* 1992). While strict radiometric control has been maintained in the processing, the component colors have not been balanced to attempt a rendition of true color. Various pseudo-color renditions which remove, to the first order, the effects of the lighting and albedo and show the distribution of different color terrains can be found in Helfenstein *et al.* (1996), Sullivan *et al.* (1996), and Veverka *et al.* (1996a,b). The subtlety of the color differences should be evident through comparison of the pseudo-color versions with the version shown here. (b) Comparative views of Ida (the HIRES mosaic, left) and Gaspra (right) showing the two asteroids at the same scale. The spatial resolution is approximately 36 m/pixel for Ida and 54 m/pixel for Gaspra. The lighting is similar in the two views: Ida's phase angle ~ 54° (actually varies from 48° to 60° across the picture); Gaspra's phase angle is 51°. The images have been filtered to enhance topographic detail. (c) Ida and Gaspra nomenclature. Names of prominent regions and features on Ida that have been either endorsed by or proposed to the International Astronomical Union. Refer to Table III for the geographical coordinates of the individual features and to Fig. 3 for the emplacement of the coordinate grid on the surface.

of Ida) and B (slightly brighter and bluer, and with a deeper 1-μm band). The spectral trends from B to A are similar to those seen on the Moon that are due to increasing soil maturity. Quantitatively, these trends are much less pronounced than those seen on the Moon (similar to lunar terrains less than 500 myr old). The most straightforward interpretation is that some of the same regolith maturation processes that occur on the Moon also occur on small asteroids, although with different time scales due to the differences in ejecta retention and mean impact velocities. Evidence that supports this interpretation is the association of terrain B with morphologically fresh craters (Sullivan *et al.* 1996) and with the inferred ejecta blanket of the large fresh crater Azzurra (Geissler *et al.* 1996).

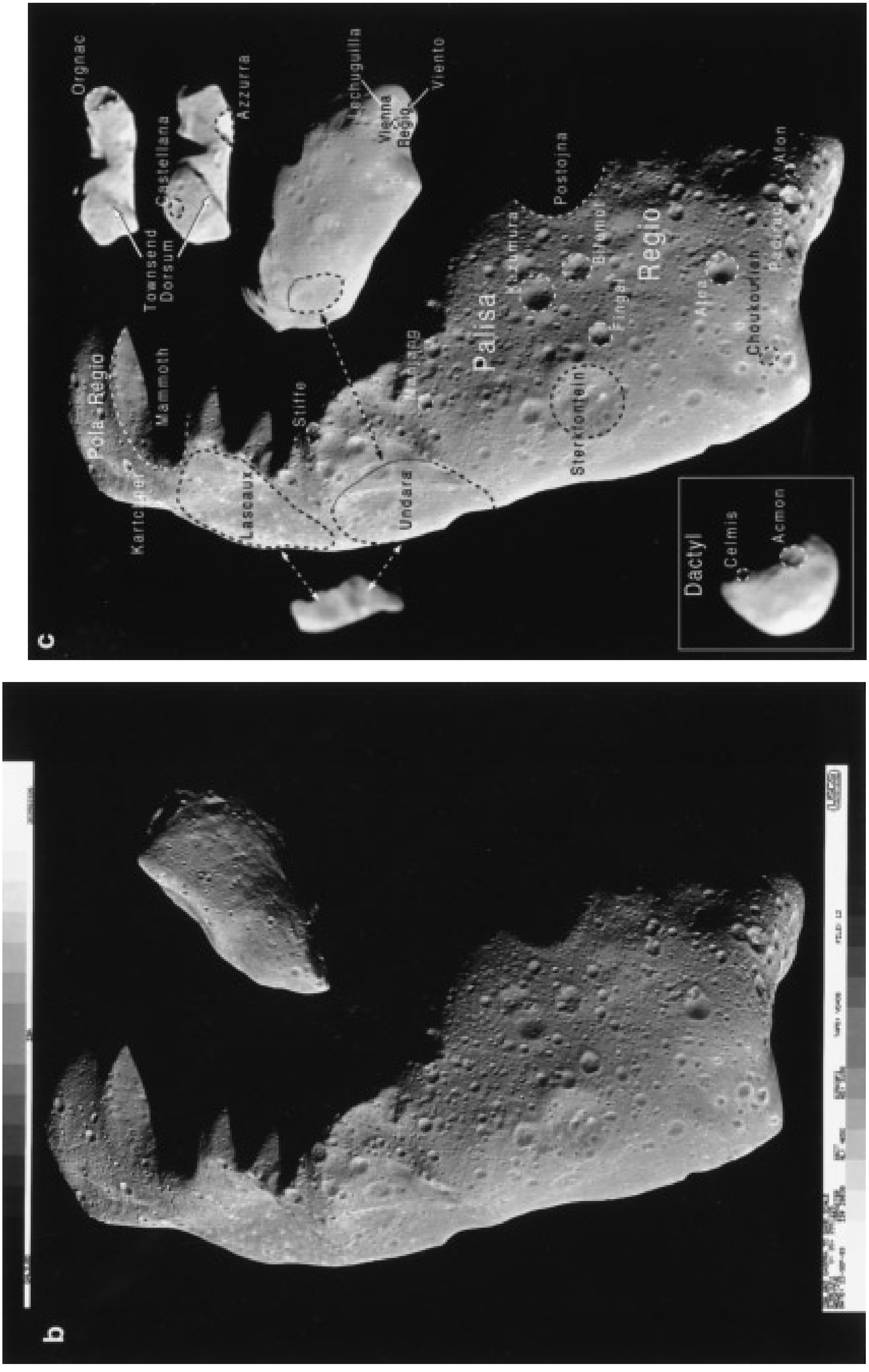

FIG. 2—*Continued*

TABLE III
Location and Size of Named Features on Ida and Dactyl

Name	Latitude	Longitude (East)	Diameter (km)	Origin	Notes
Ida Craters					
Afon	-6.4	0.0	0.8	Russia	Origin of longitude system on Ida.
Atea	-5.7	18.9	2.0	Papua, New Guinea	Cave in the Mutler Range
Azzurra	30.5	217.2	9.6	Italy	Flooded cave (known as the Blue Grotto on the island of Capri. Accessible by boat.
Bilemot	-27.8	29.2	1.8	Korea	Lava tube.
Castellana	-13.4	335.2	5.2	Puglia region, Italy	Cave rich in depositional features.
Choukoutien	12.8	23.6	1.1	China	Site of discovery of "Peking Man."
Fingal	-13.2	39.9	1.5	Hebrides, Scotland	Noted for sound created by water and wind.
Kartchner	-7.0	179.0	0.9	Arizona, USA	Pristine cavern opened 1988.
Kazumura	-32.0	41.1	2.1	Hawaii	Lava tube.
Lascaux	0.8	161.2	11.8	France	Noted for prehistoric paintings.
Lechuguilla	7.9	357.1	1.5	New Mexico, USA	Cave with no natural openings.
Mammoth	-18.3	180.3	10.2	Kentucky, USA	Longest limestone cave known.
ManJang	-28.3	90.5	1.0	Korea	Lava tube.
Orgnac	-6.3	202.7	10.6	France	Cave more than 1 million y old.
Padirac	-4.3	5.2	1.9	France	Cave with underground river.
Postojna	-42.9	359.9	~6.0	Slovenia	
Sterkfontein	-4.1	54.1	4.7	South Africa	Archeological site.
Stiffe	-27.9	126.5	1.5	Sulmona, Italy	Karst cave.
Undara	2.0	113.8	8.5	Australia	Longest known lava tube system. From Undara Volcano
Viento	12.2	343.9	1.6	Canary Islands	Lava tube.
Ida Regii					
Palisa regio	-23	34	~23	-	Named for Ida's discoverer Johann Palisa (1848 - 1925)..
Pola regio	-10	-185	-	-	Palisa observed at Pola
Vienna regio	8	0	-	-	Palisa observed from Vienna where he discovered Ida.
Ida Dorsa					
Townsend Dorsum	25	30	-	-	The late Tim Townsend was manager and developer of the SSI Home Institution Image Processing System.
Dactyl Craters					
Acmon	-39	138	0.3	-	One of the original three Dactyls.
Celmis	-46	220	0.16	-	One of the original three Dactyls .

The spectrum of Dactyl is similar to but definitely different from the two endmember color units on Ida. Veverka *et al.* (1996b) argue that the explanation of this color difference is likely to be different from the reason that accounts for the difference between the two color terrains on Ida, i.e., optical maturation. They find that textural differences are also unlikely to be responsible and suggest that Dactyl's spectrum may reflect a compositional difference with Ida—a slight enrichment of pyroxene in its compositional makeup relative to Ida. Another possible explanation of the small spectral differences, or some part of these differences, between Dactyl and Ida is from a currently poorly understood "space weathering" process that slightly modifies the color of the surface with time (Chapman *et al.* 1995a).

Whether the portion of the Koronis parent body that became Ida was differentiated or undifferentiated (e.g., chondritic) is the subject of current debate. Ida's low bulk density, and suggestions that Ida may have a structurally intact central interior (Asphaug *et al.* 1996), would be inconsistent with metal-rich stony-iron compositions some have proposed as analogs for S-type asteroids. But they would be consistent with dominantly stony compositions, either chondritic or achondritic (Belton *et al.* 1995). Although "ordinary" chondrites are 10 times more common than achondrites among observed meteorite falls (Sears and Dodd 1988), this still may be a biased sample of main belt asteroid compositions (Bell *et al.* 1989). Spectral studies of the Koronis asteroid family show strong similarities from body to body, but with some possible mineralogical variations (Binzel *et al.* 1993b). Nevertheless, most of the Koronis asteroids do have an olivine:orthopyroxene ratio similar to the chondrites, so it is conceivable that Ida was born from a large undifferentiated portion of the Koronis parent body.

If the Koronis parent body were differentiated, then we might hope to see evidence of compositional heterogeneity on Ida (despite widespread homogenization by ejecta), but there is no clear evidence for such heterogeneity in the SSI data. The most sensitive test for heterogeneity is the 889/990 nm ratio, which would vary spatially if a nonuniform distribution of Ca, Fe, and Mg abundances in pyroxenes or in olivine in the olivine:pyroxene ratio were present. The 889/990 nm ratio images are in fact very uniform, and the small variations present are most likely due to noise. Even in the presence of a globally homogenized regolith, the recent craters might reveal compositional heterogeneity. The craters appear uniform in the 889/990 nm ratio, but do vary in the less mineralogically diagnostic parameters of color, albedo, and 1-μm band depth. Most of this variation is consistent with regolith maturity variations (cf. Geissler *et al.* 1996, Helfenstein *et al.* 1996, Sullivan *et al.* 1996, Veverka *et al.* 1996b).

The only possible evidence for compositional heterogeneity in the SSI data comes from the presence and distribution of dark-floored craters. Dark-floored craters are spectrally similar to the surrounding material and distinguished by their lower albedo. They are clearly identified only in a single location near one end of Ida, but this may be partly an observational artifact in which dark floors are only seen where there is both a favorable photometric geometry (low phase and emission angles) and relatively high spatial resolution (Sullivan *et al.* 1996). We have considered here two leading models for the origin of the dark floors: (1) exposure of a darker underlying layer in some regions, suggestive of compositional heterogeneity; and (2) concentrations of impact melt. Both models have difficulties.

Geissler *et al.* (1996) find that two significant observed facts about Ida, the presence of positive relief features (interpreted as ejecta blocks) on the most elongated "ends" of Ida (Lee *et al.* 1996) and a large Terrain B color unit near Ida's north polar region, can be elegantly explained as the result of a relatively recent large impact event which formed the large fresh crater Azzurra (Fig. 2c). Although this crater is present near the margin of the color unit, and we initially expected ejecta blankets to be either bilaterally or radial symmetric about a crater from our previous observations on larger bodies, Geissler *et al.* (1996) show that the effects of Ida's rapid rotation, irregular shape, and low gravity can result in highly asymmetric ejecta deposits. Using realistic physical models for Ida, they show that the Azzurra impact was probably responsible for both the large blue unit (immature soil exposed by reaccretion of ejecta) and the presence and distribution of blocks on Ida's rotational leading surfaces (Azzurra ejecta launched in the direction of rotation and swept up by Ida). This result demonstrates that spectral variations seen in rotational lightcurves (Binzel *et al.* 1993) may not be evidence for compositional heterogeneity, as has been generally assumed. This provides an excellent example of how spacecraft observations of a single object can help improve the interpretations of ground-based observations of a much larger number of asteroids.

RELATIONSHIPS WITH GASPRA AND AGE RELATIONSHIPS

It seems clear that the Galileo imaging observations of these two small bodies give quite different and, in some aspects, complementary views of cratering and regolith processes operating in the asteroid belt. On Gaspra (cf. Veverka *et al.* 1994) we found an unsaturated crater density distribution and signs of a relatively recent global "resetting" of the cratering record (Carr *et al.* 1994, Greenberg *et al.* 1994). On Ida, where some expectations were for a very young surface (from astronomical data on the Koronis family (Binzel 1988)), we would normally interpret the cratering record to imply a very old surface in saturation equilibrium except, perhaps, for the largest craters (Chapman *et al.,* 1996). Yet, Ida is orbited by tiny Dactyl whose collisional destruction time scale must be very short (Davis *et al.,* 1996) and the surface of Ida is littered with large blocks (Lee *et al.* 1996, Geissler *et al.* 1996) that may, or may not (Lee *et al.* 1996), be similarly short lived. This situation calls for novel alternative explanations of the collisional history and cratering record such as that presented in Greenberg *et al.* (1996), and by Chapman *et al.* (1996).

Terrains that have similar microphysical properties occur on both Gaspra and Ida (Veverka *et al.* 1996b). However, they also show markedly different correlations with topography. On Ida no global correlation between color and slope elevations is evident, while on Gaspra the reverse is true. One explanation is that Ida has a deeper regolith (Sullivan *et al.* 1996), including blanketing by the Azzurra (Geissler *et al.* 1996) and similar events.

LESSONS AND OBJECTIVES FOR FUTURE EXPLORATION

The Gaspra and Ida flybys hold important lessons for the design of future flyby missions. The importance of obtaining accurate shape information for irregular bodies, the fundamental significance of obtaining accurate knowledge of the spin state (usually requiring a substantial ground-based program adequately endowed with observing time), and the need for an accurately calibrated *inflight* system cannot be overly stressed.

These requirements should be drivers in the design of future flyby imaging systems. Adequate knowledge of shape in flybys requires a high-angular-resolution (2.5–5 μradian/pixel) camera to provide adequate resolution over at least a full rotation period of the target. It does not seem to be well known that this requirement on the angular resolution of a camera is as significant in practice as the ever present demands of high-resolution mapping at the time of the encounter itself. Photometric accuracy in the inflight system places further demands on performance,

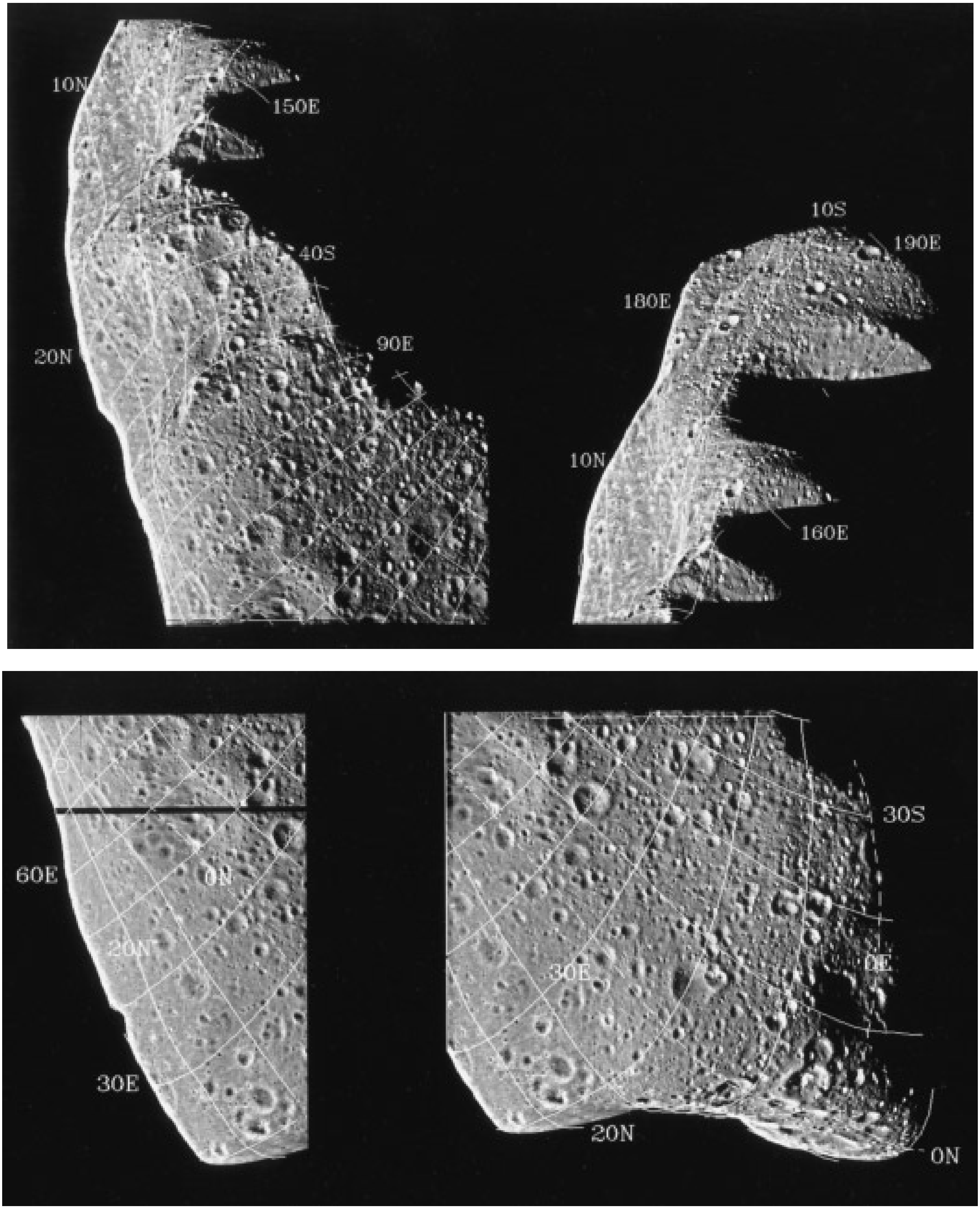

FIG. 3. High-resolution views of Ida with the control net coordinate grid superimposed (Thomas *et al.* 1996, Davies *et al.* 1996). Because of the extreme irregularity of Ida's shape, the identification and interpolation of coordinate positions of features on the surface are not always obvious. In the full frame views the subsolar and subspacecraft locations are marked with a circle and a cross respectively.

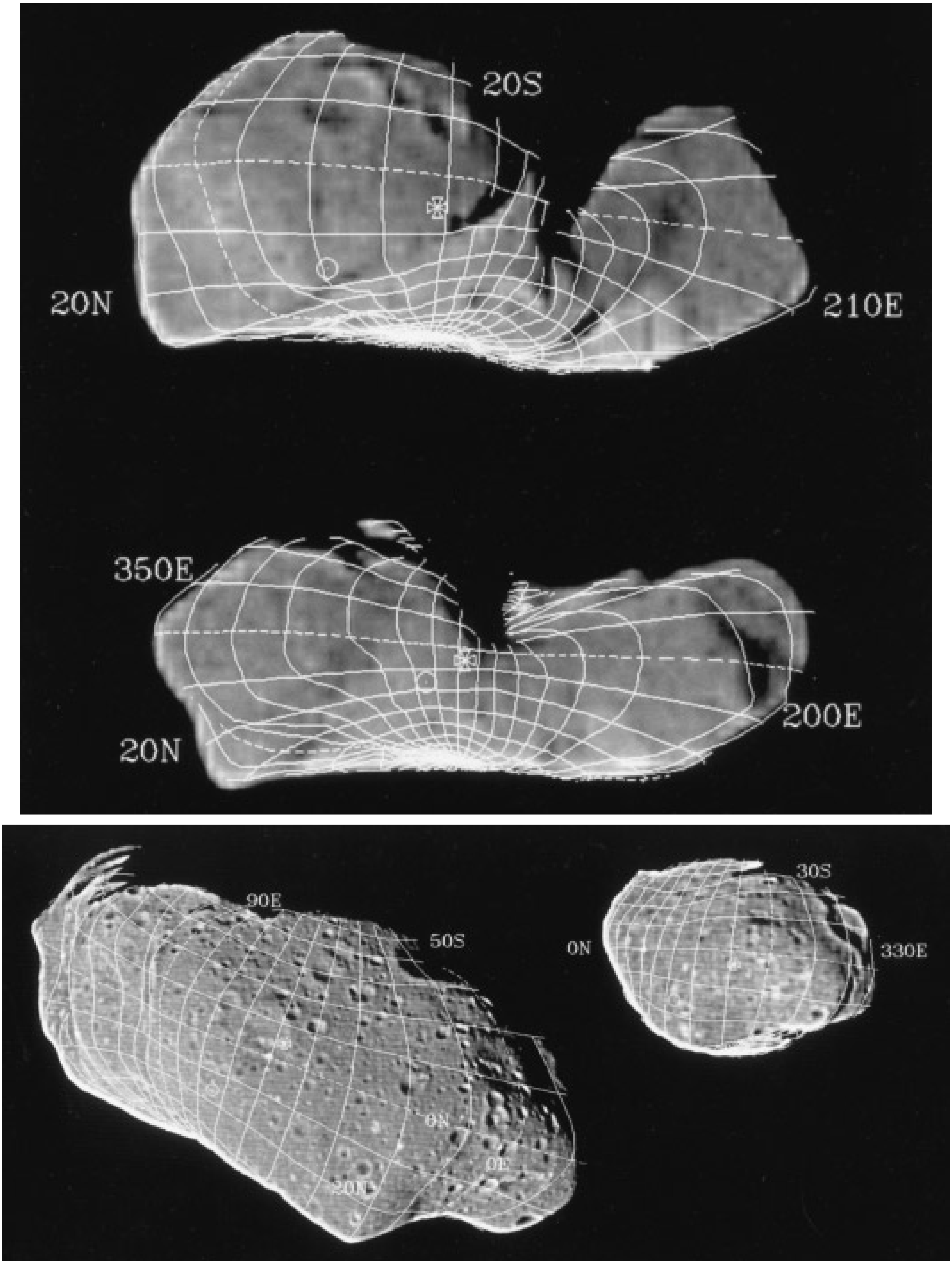

FIG. 3—*Continued*

this time leading to a need to employ large format detectors (i.e., arrays with $> 10^6$ pixels) and increased demand for onboard data storage. With hindsight, it is quite clear to us that a design with the detector pixel size matched to the optical point spread function (psf), as in the Galileo camera, would be difficult to calibrate inflight using standard stellar sources as was our experience. Oversampling of the psf should be a feature of future systems. Similarly, the antiquated "standard" of 8-bit linear encoding is inadequate for the digitization of the signal from modern detectors. Such provisions, and others, would guarantee that the precision inflight calibrations that are essential for a fully quantitative experiment, and which, preferably by utilizing flat fields internal to the instrument, can be accomplished efficiently and with the minimum difficulty.

A severe (and expensive) limitation of the Galileo system was experienced in the process of integrating the operation of different instruments that are fundamentally synergistic in the scientific use of their data, but were not designed to work well together. This is a particular problem for SSI and NIMS. In the future visible imagers and near-IR imaging spectrometers should be designed to operate together and not (effectively) sequentially. The future demands instrumental *innovation.*

Finally, the well-used practice of sequencing science activities "open-loop," i.e., using near-real time optical navigation updates to preplanned instrument sequences that have only probabilistic information of the position of the target with time, is now enormously restrictive and wasteful of resources both fiscally and in terms of onboard data storage. Smart, automatic "lock-on," target acquisition systems are now available that should make open-loop concepts obsolete. Such systems can guarantee efficient imaging *at* closest approach and simultaneously allow approach distances to be appreciably lowered. Greatly increased spatial resolution on the surface and increased instrument compatibility should ensue.

Some important asteroid objectives can be accomplished only with rendezvous missions, perhaps including *in situ* probes, or sample return missions. However, high-resolution observations with meaningful sampling statistics for a variety of spectral types and over a range of asteroid sizes can potentially be accomplished at reasonable cost only by flyby missions. Options include relatively large spacecraft that fly by multiple targets or that fly by one or two asteroids en route to another final destination (e.g., Galileo, possibly Cassini, and Rosetta), many small low-cost spacecraft such as proposed as Discovery missions (Belton and Delamere 1992), or microspacecraft as in NASA's New Millennium concept.

We offer the following list of desirable capabilities and remote-sensing instrumentation for future asteroid flyby missions:

1. Lock-on, autonomous navigation and instrument pointing so that continuous imaging is possible throughout very close flybys (100 km) without expensive open-loop optical navigation, sequence integration, and wasteful mosaicking searching for the target. This should also enable Doppler tracking at a sensitivity that will allow accurate mass determinations and provide useful constraints on bulk densities.
2. High-angular-resolution (~2.5–5 μradians/pixel), large pixel format CCD imaging system (possibly integrated with a near-IR spectral mapper) for medium resolution (100 m) imaging of illuminated regions rotated away from the spacecraft at closest approach, as well as meter-scale imaging near closest approach at 100-km range. The detector should oversample the optical psf to ensure accurate inflight calibration.
3. Visible/near-IR (0.4–5.0 μm) imaging spectrometer with sufficient spatial resolution to determine the mineralogy of many small craters formed in the strength regime (~100 m/pixel for Ida). Simultaneous, or near-simultaneous, observation in all spectral bands is needed to avoid difficult registration problems due to the rapidly changing geometry of fast flybys. Conceptual designs that integrate visible, and near-IR and visible spectral imaging have already been proposed for Discovery missions. Once again the use of technical innovation is the key element.
4. Thermal-IR imaging with a long focal length (>0.5 m) is needed for high-resolution imaging of asteroid regions in shadow during the close flyby, and for determinations of thermal inertia. The system must be sensitive down to about 150 K.

Active experiments such as artificial impacts may be the only way to constrain internal properties via flyby missions. Two microspacecraft might be used for this purpose, one to impact the asteroid and the second to observe the effects.

ACKNOWLEDGMENTS

We recognize and applaud the superb performance of all elements of the Galileo Project Flight Teams responsible for the detailed planning and execution of the Ida encounter under the direction of William O'Neil, Neil Ausman, Torrence Johnson, Robert Mitchell, and Karen Buxbaum who worked so extremely hard and creatively. In particular we recognize their professionalism in recovering from the spacecraft control anomaly on approach and the creation and execution of the adaptive data acquisition strategy that allowed all relevant data to be returned prior to the use of the tape recorder for observations of the impacts of Comet Shoemaker–Levy 9 into Jupiter's atmosphere.

We also thank Jan Ludwinski, Karen Carr, Brian Marsden, and those members of the IAU nomenclature committees who were of great assistance in finding a suitable nomenclature for Ida and Dactyl in time for the publication of this special issue. The National Optical Astronomy Observatories are operated by AURA, Inc. for the National Science Foundation. This research was supported by the National Aeronautics and Space Administration through the Jet Propulsion Laboratory Galileo Project.

REFERENCES

Asphaug, E., J. M. Moore, D. Morrison, W. Benz, M. C. Nolan, and R. J. Sullivan 1996. Mechanical and geological effects of impact cratering on Ida. *Icarus* **120,** 158–184.

Bell, J. F., D. R. Davis, W. K. Hartmann, and M. J. Gaffey 1989. Asteroids: The big picture. In *Asteroids II* (R. P. Binzel, T. Gehrels, and M. S. Matthews, Eds.), pp. 921–948. Univ. of Arizona Press, Tucson.

Belton, M. J. S., and A. Delamere 1992. Low cost missions to explore the diversity of near Earth objects. In *Proceedings of Asteroids, Comets, Meteors Conference* (A. W. Harris and E. Bowell, Eds.). Lunar and Planetary Institute, Houston.

Belton, M. J. S., K. P. Klaasen, M. C. Clary, J. L. Anderson, C. D. Anger, M. H. Carr, C. R. Chapman, M. E. Davies, R. Greeley, D. Anderson, L. K. Bolef, T. E. Townsend, R. Greenberg, J. W. Head III, G. Neukum, C. B. Pilcher, J. Veverka, P. J. Gierasch, F. P. Fanale, A. P. Ingersoll, H. Masursky, D. Morrison, and J. B. Pollack 1992. The Galileo solid state imaging experiment. *Space Sci. Rev.* **60**, 413–455.

Belton, M. J. S, and R. Carlson 1994. 1993 (243) 1. *IAU Circular* 5948.

Belton, M. J. S., C R Chapman, J. Veverka, K. P. Klaasen, A. P. Harch, R. Greeley, R. Greenberg, J. W. Head III, A. S. McEwen, D. Morrison, P. C. Thomas, M. E. Davies, M. H. Carr, G. Neukum, F. P. Fanale, D. R. Davis, C. Anger, P. Gierasch, A. P. Ingersoll, and C. B. Pilcher 1994. First images of Asteroid 243 Ida. *Science*, **265**, 1543–1547.

Belton, M. J. S., C. R. Chapman, P. C. Thomas, M. E. Davies, R. Greenberg, K. Klaasen, D. Byrnes, L. D'Amario, S. Synnott, T. V. Johnson, A. McEwen, D. R. Davis, W. Merline, J.-M. Petit, A. Storrs, J. Veverka, B. Zellner, and the Galileo Imaging Team 1995a. The bulk density of the asteroid 243 Ida from Dactyl's orbit. *Nature* **374,** 785–788.

Belton, M. J. S., B. E. A. Mueller, L. A. D'Amario, D. V. Byrnes, K. P. Klaasen, S. Synnott, H. Breneman, T. V. Johnson, P. C. Thomas, J. Veverka, A. P. Harch, M. E. Davies, W. Merline, C. R. Chapman, D. R. Davis, T. Denk, G. Neukum, J.-M. Petit, R. Greenberg, A. Storrs, and B. Zellner 1996. The discovery and orbit of 1993 (243)1Dactyl. *Icarus* **120,** 185–199.

Binzel, R. P. 1988. Collisional evolution in the Eos and Koronis families: Observational and numerical results. *Icarus* **73**, 303–313.

Binzel, R. P., S. M. Slivan, P. Magnusson, W. Wisniewski, J. Drummond, K. Lumme, M. A. Barucci, E. Dotto, C. Angeli, D. Lazzaro, S. Mottola, M. Gonano-Breurer, T. Michalowski, G. De Angelis, D. J. Tholen, M. Di Martino, M. Hoffmann, E. Geyer, and F. Velichko 1993a. Asteroid 243 Ida: Groundbased photometry and a pre-Galileo physical model. *Icarus* **105**, 310–325.

Binzel, R. P., S. Xu, and S. J. Bus 1993b. Spectral variations within the Koronis family: Possible implications for the surface colors of asteroid 243 Ida. Icarus **106**, 608–611.

Carr, M. H., R. L. Kirk, A. McEwen, J. Veverka, P. Thomas, J. W. Head, and S. Murchie 1994. The geology of Gaspra. *Icarus* **107**, 61–71.

Chapman, C. R., J. Veverka, P. C. Thomas, K. Klaasen, M. J. S. Belton, A. Harch, A. McEwen, T. V. Johnson, M. E. Davies, W. J. Merline, and T. Denk 1995a. Discovery of a satellite of Asteroid 243 Ida and its physical properties. *Nature* **374,** 783–785.

Chapman, C. R., W. J. Merline, K. Klaasen, T. V. Johnson, C. Heffernan, M. J. S. Belton, A. P. Ingersoll, and the Galileo Imaging Team 1995b. Preliminary results of *Galileo* direct imaging of S–L 9 impacts. *Geophys. Res. Lett.* **22,** 1561–1565.

Chapman, C. R., E. V. Ryan, W. J. Merline, G. Neukum, R. Wagner, P. C. Thomas, J. Veverka, and R. J. Sullivan 1996. Cratering on Ida. *Icarus* **120,** 77–86.

D'Amario, L., L. Bright, D. Byrnes, J. Johannesen, and J. Ludwinski 1989. VEEGA mission description. In *AAS/AIAA Astrodynamics Specialist Conference, Vermont, Aug. 1989*. AAS Publication Office.

Davies, M. E., T. R. Colvin, M. J. S. Belton, J. Veverka, and P. C. Thomas 1996. The direction of the North Pole and the control network of asteroid 243 Ida. *Icarus* **120**, 33–37.

Davis, D. R., C. R. Chapman, D. D. Durda, P. Farinella, and F. Marzari 1996. The formation and collisional/dynamical evolution of the Ida/Dactyl system as part of the Koronis family. *Icarus* **120**, 220–230.

Durda, D. D. 1996. The formation of asteroidal satellites in catastrophic collisions. *Icarus* **120**, 212–219.

Gaffey, M. J., J. F. Bell, R. H. Brown, T. H. Burbine, J. L. Piatek, K. L. Reed, and D. A. Chaky 1993. Mineralogical variation within the S-type asteroid class. *Icarus* **106**, 573–602.

Geissler, P., J.-M. Petit, D. Durda, R. Greenberg, W. Bottke, M. Nolan, and J. Moore 1996. Erosion and ejecta reaccretion on 243 Ida and its moon. *Icarus* **120**, 140–157.

Greenberg, R., M. C. Nolan, W. F. Bottke, Jr, R. A. Kolvoord, and J. Veverka 1994. Collisional history of Gaspra. *Icarus* **107**, 84–97.

Greenberg, R., W. Bottke, M. Nolan, P. Geissler, J.-M. Petit, D. Durda, E. Asphaug, and J. Head 1996. Collisional and dynamical history of Ida. *Icarus* **120**, 106–118.

Helfenstein, P., J. Veverka, P. C. Thomas, D. P. Simonelli, K. Klaasen, T. V. Johnson, F. Fanale, J. Granahan, A. S. McEwen, M. Belton, and C. Chapman 1996. Galileo photometry of asteroid 243 Ida. *Icarus* **120**, 48–65.

Lee, P., J. Veverka, P. C. Thomas, P. Helfenstein, M. J. S. Belton, C. R. Chapman, R. Greeley, R. T. Pappalardo, R. Sullivan, and J. W. Head III 1996. Ejecta Blocks on 243 Ida and on other asteroids. *Icarus* **120**, 87–105.

Neukum, G., G. Hahn, T. Denk, M. J. S. Belton, C. R. Chapman, I. Nemtchinov, N. Artem'eva, V. Chouvalov, I. Kosarev, and V. Svettsov 1995. The collisional modeling of Comet Shoemaker–Levy 9 with Jupiter as seen by the Galileo Imaging Experiment: Modeling and interpretation of the bolide and explosion phase. In *Proceedings European SL–9/Jupiter Workshop* (R. West and H. Boehnhardt, Eds.). ESO Publication.

Sears, D. W. G., and R. T. Dodd 1988. Overview and classification of meteorites. In *Meteorites and the Early Solar System* (J. F. Kerridge and M. Shapley Mathews, Eds.), pp. 3–31. Univ. of Arizona Press, Tucson.

Simonelli, D. P., J. Veverka, P. C. Thomas, P. Helfenstein, B. T. Carcich, and M. J. S. Belton 1996. Ida lightcurves: Consistency with Galileo shape and photometric models. *Icarus* **120**, 38–47.

Sullivan, R., R. Greeley, R. Pappalardo, E. Asphaug, J. M. Moore, D. Morrison, J. Moore, M. J. S. Belton, M. Carr, C. R. Chapman, P. Geissler, R. Greenberg, J. Granahan, J. W. Head III, R. Kirk, A, McEwen, P. Lee, P. C. Thomas, and J. Veverka 1996. Geology of 243 Ida. *Icarus* **120**, 119–139.

Thomas, P. C., M. J. S. Belton, B. Carcich, C. R. Chapman, M. E. Davies, R. Sullivan, and J. Veverka 1996. The shape of Ida. *Icarus* **120**, 20–32.

Veverka, J., M. Belton, K. Klaasen, and C. Chapman 1994. Galileo's encounter with 951 Gaspra: Overview. *Icarus* **107**, 2–17.

Veverka, J., P. C. Thomas, P. Helfenstein, P. Lee, A. Harch, S. Calvo, C. Chapman, M. J. S. Belton, K. Klaasen, T. V. Johnson, and M. Davies 1996a. Dactyl: Galileo observations of Ida's satellite. *Icarus* **120**, 200–211.

Veverka, J., P. Helfenstein, P. Lee, P. Thomas, A. McEwen, M. Belton, K. Klaasen, T. V. Johnson, J. Granahan, F. Fanale, P. Geissler, and J. W. Head III 1996b. Ida and Dactyl: Spectral reflectance and color variations. *Icarus* **120**, 66–76.